PHYSICAL REVIEW A, VOLUME 64, 033407

# Experimental study of the quantum driven pendulum and its classical analog in atom optics

W. K. Hensinger,[1] A. G. Truscott,[1] B. Upcroft,[1] M. Hug,[1] H. M. Wiseman,[1,2] N. R. Heckenberg,[1] and H. Rubinsztein-Dunlop[1]
[1]*Centre for Laser Science, Department of Physics, The University of Queensland, Brisbane, Queensland 4072, Australia*
[2]*School of Science, Griffith University, Nathan, Brisbane, Queensland 4111, Australia*
(Received 30 August 2000; published 6 August 2001)

We present experimental results for the dynamics of cold atoms in a far detuned amplitude-modulated optical standing wave. Phase-space resonances constitute distinct peaks in the atomic momentum distribution containing up to 65% of all atoms resulting from a mixed quantum chaotic phase space. We characterize the atomic behavior in classical and quantum regimes and we present the applicable quantum and classical theory, which we have developed and refined. We show experimental proof that the size and the position of the resonances in phase space can be controlled by varying several parameters, such as the modulation frequency, the scaled well depth, the modulation amplitude, and the scaled Planck's constant of the system. We have found a surprising stability against amplitude noise. We present methods to accurately control the momentum of an ensemble of atoms using these phase-space resonances which could be used for efficient phase-space state preparation.

DOI: 10.1103/PhysRevA.64.033407 PACS number(s): 32.80.Pj, 05.45.Mt, 42.50.Vk

## I. INTRODUCTION

The field of ''quantum chaos'' was born in 1917 when Albert Einstein tried to unravel which mechanical systems could be subjected to the Bohr-Sommerfeld-Epstein quantization rules [1]. He concluded that in the absence of invariant tori in phase space these quantization rules cannot be used and that, moreover, this absence applies to most systems. Chaos is associated with a rapid divergence of arbitrarily close points in phase space [2]. Strictly speaking there can be no such thing as quantum chaos as an infinitely fine level of detail is needed to describe the trajectories of a classical chaotic system. In reality a system is bound by Heisenberg's uncertainty principle restricting the amount of detail of position and momentum needed for classical chaos. Classical chaos can be described as the emergence of complexity on infinitely fine scales in classical phase space. In contrast, in quantum mechanics structure is smoothed away in an area below the size of $\hbar$ [2,3].

During the years since the birth of quantum chaos, significant amounts of theory have been created to give a better description of chaotic physical systems in a quantum dynamical context. The key question is, what happens to classical chaos in the quantum world? One approach is to seek generic features of quantum dynamics for a system whose classical description exhibits chaotic dynamics. One example of such features is dynamical localization, a quantum suppression of classical diffusion, which was discovered by Fishman *et al.* [4] in numerical studies of the periodically kicked quantum rotor. Conductance fluctuations in ballistic microstructures associated with complex electron trajectories constitute another example of the occurrence of quantum chaos [5]. Finally, molecular excitation experiments can show interesting quantum features (e.g., Anderson localization, an effect related to dynamical localization) if the scaled Planck's constant is kept finite but exhibits chaotic dynamics in the classical limit ($\hbar=0$) [6]. To gain a different perspective on the quantum nature of classical chaos some experiments look at the manifestations of classical chaos in wave propagation. In these experiments the time-independent wave equation, the Helmholtz equation, is mathematically equivalent to the time-independent Schrödinger equation for a billiard system. In billiard-shaped cavities eigenfrequencies and eigenfunctions can be measured by microwave absorption. In 1991 quantum scars, which are concentrations of probability along periodic orbits, were experimentally observed by Sridhar [7]. Experiments to study the quantum dynamics of classically chaotic systems have been carried out on Rydberg atoms, measuring microwave ionization of highly excited hydrogen atoms [8,9]. One result of these experiments is the recognition of different regimes determined by how well classical and quantum mechanics agree with each other. These regimes are characterized by the scaled microwave frequency given by $\Omega_0=n_0\Omega$, where $n_0$ is the principal quantum number of the initial state and $\Omega$ the microwave frequency.

It was first proposed by Graham, Schlautmann, and Zoller [10] to use atom manipulation experiments to test predictions of quantum chaos. Cold atoms provide new grounds for experiments in quantum chaos which have some advantages compared to Rydberg atom experiments. First, the potentials that are used are extremely well approximated as one-dimensional potentials. In contrast, the potentials involved in the Rydberg-atom ionization experiments are much harder to approximate by one-dimensional potentials. At present the three-dimensional quantum simulations needed for these highly excited atoms are not feasible without severe approximations [9]. Second, in atom optics there is considerable control over the potentials. In the Rydberg-atom case the Coulomb potential dictates the dynamics and the system is complicated due to electron-electron interactions (the chaotic trajectory of the outer electron in a Rydberg atom can closely approach the shell of inner electrons). In atom optics one can tailor the potentials to match the theoretical description and indeed achieve simple nonlinear potentials such as the nonlinear pendulum which we consider in this study. We can also achieve a considerable variety of modulation dynamics. Finally, atom-optical systems are far less dissipative and

 

noisy than Rydberg-atom experiments due to laser cooling and the ability to operate far off resonance. Hence atom-optical systems can be well approximated by Hamiltonian dynamics.

Moore *et al.* [11] and Ammann *et al.* [12] showed that cold atoms can be used to simulate the quantum delta kicked rotor (Q-DKR). Raizen's group also reported the experimental observation of dynamic localization in cold atoms [13] which is the quantum suppression of chaotic diffusion. It can be roughly understood by considering that classical chaotic paths can interfere destructively. Decoherence will tend to suppress this quantum behavior and leads to classical-like dynamics.

Our group has recently demonstrated the existence of phase space resonances for the quantum driven pendulum (QDP) in cold atoms that we report on in this paper. Although it is probably the first time that such phase-space resonances have been observed for the QDP, Raizen and coworkers had previously observed momentum distributions that are due to atoms being trapped in a first-order resonance in the dynamics of cold atoms in a phase-modulated standing wave [14]. This particular first-order resonance corresponds to the central elliptic fixed point at the origin of phase space. In contrast we are investigating second-order resonances for the QDP, which are distinct features in the momentum distribution of cold atoms traveling with a nonzero mean velocity on top of a background of atoms moving chaotically in phase space.

Phase-space resonances have also been seen in other physical systems. For example, they have been reported in plasma physics. Sinclair, Hosea, and Sheffield [15] mapped a toroidal magnetic field in a stellarator using phase stabilized electrons. Islands of stability emerged in the phase-space dynamics of the electrons. In fluid flow experiments particle motion in the fluid was shown to have chaotic and regular phase-space regions [16]. In experiments on microwave ionization of Rydberg atoms strong classical resonance effects in the final-bound-state quantum number distribution were found by Bayfield and Sokol [17]. These peaks cannot be associated with any quantum-mechanical resonance transition [9].

Atom-optics experiments provide a good opportunity to examine the transition between classical and quantum mechanics. Dyrting and co-workers [18] made a theoretical study of cold atoms which are subjected to a single-frequency amplitude-modulated standing wave. They predicted quantum tunneling between phase-space resonances for this system. Hug and Milburn [19] showed that quantum-mechanical velocity predictions for second-order phase-space resonances disagree by up to 20% with classical predictions in the quantum driven pendulum [20].

We analyze in this study the phase-space resonances that we found in the dynamics of the experimental realization of the quantum driven pendulum and its classical analog with cold atoms and test theoretical predictions. The system shows either classical or quantum behavior, depending on the parameters chosen for the system. In the context of this study we mean by quantum behavior a situation where a classical simulation cannot predict some of the observed experimental features while a quantum simulation can. This constitutes the importance of the system for quantum chaos studies. We also analyze here the observed second-order phase-space resonances in detail. We present experimental findings showing how they can be manipulated and how to momentum control them. We give an overview of the resonance dynamics for different parameter regimes to characterize the atomic dynamics qualitatively and quantitatively. A surprising range of dynamics arises. Furthermore, we present methods for efficient momentum phase-space state preparation utilizing the quantum chaotic phase space of the QDP. This could have a variety of applications in atom optics, for example beam splitters and atomic interferometry. Furthermore, we will show introductory results on how noise affects the system.

## II. DESCRIPTION OF THE QUANTUM DRIVEN PENDULUM AND ITS CLASSICAL ANALOG

Our QDP experiments have been carried out using cold rubidium atoms that are positioned in a far detuned optical standing wave. Modulation of the intensity of the standing wave leads to an effective Hamiltonian for the center-of-mass motion (as shown in the Appendix) given by

$$H=\frac{p_x^2}{2m}+\frac{\hbar\Omega_{\mathrm{eff}}}{4}(1-2\varepsilon\sin\omega t)\sin^2(kx), \tag{1}$$

where the effective Rabi frequency is $\Omega_{\mathrm{eff}}=\Omega^2/\delta$, $\Omega=\Gamma\sqrt{I/I_{\mathrm{sat}}}$ is the resonant Rabi frequency, $\varepsilon$ is the modulation parameter, $\omega$ is the modulation angular frequency, $\Gamma$ is the inverse spontaneous lifetime, $\delta$ is the detuning of the standing wave, $t$ is the time, and $p_x$ the momentum component of the atom along the standing wave. Here $I$ is the spatial mean of the intensity of the unmodulated standing wave (which is half of the peak intensity so $\Omega=\Gamma\sqrt{I_{\mathrm{peak}}/2I_{\mathrm{sat}}}$) and $I_{\mathrm{sat}}$ is the saturation intensity. Using scaled variables [11] the Hamiltonian is given by

$$\mathcal{H}=p^2/2+2\kappa(1-2\varepsilon\sin\tau)\sin^2(q/2), \tag{2}$$

where $\mathcal{H}=(4k^2/m\omega^2)H$, $q=2kx$, $p=(2k/m\omega)p_x$ and $k$ is the wave number. The driving amplitude is given by

$$\kappa=\omega_r\Omega_{\mathrm{eff}}/\omega^2=\frac{\hbar k^2\Omega_{\mathrm{eff}}}{2\omega^2 m}, \tag{3}$$

where $\omega_r=\hbar k^2/2m$ is the recoil frequency and $\tau=t\omega$ is the scaled time variable. The commutator is given by

$$[p,q]=i\bar{k}, \tag{4}$$

where the scaled Planck's constant is $\bar{k}=8\omega_r/\omega$. This system can be seen to be equivalent to a driven pendulum, because the Hamiltonian is equivalent to that of an amplitude-driven pendulum [18].

The system exhibits classical and quantum-mechanical regimes determined by the value of the scaled Planck's constant $\bar{k}$ [10]. To understand the nature of the resonances it is best to estimate first when they can be treated classically and

when one has to use a full quantum simulation to predict the dynamics of the system. The scaled Planck's constant can be rewritten as

$$k=\frac{4\hbar k^2}{\omega m}=4\hbar\frac{4\pi^2}{\lambda^2\omega}=4\hbar\pi^2\left(\frac{1}{\frac{\lambda}{2}\left(\frac{\lambda}{2T}m\right)}\right)=\frac{4\hbar\pi^2}{2\pi I_0}=\frac{h}{I_0}, \tag{5}$$

where $T$ is the modulation period, $\hbar$ is Planck's constant, $\lambda$ is the wavelength, and $I_0$ is the action of a free particle over the distance $\lambda/2$ in the time $T$. Our one-dimensional system can be described in the corresponding two-dimensional phase space which is spanned by momentum and position coordinates. The position coordinate axis is orientated along the standing wave. The action of the system, multiplied by $2\pi$, is given by the area in phase space, which is encircled by the trajectory of a particle. $k$ can be interpreted as the ratio of Planck's constant to the action of a particle in the system described. Now if the phase-space area of a resonance is on the same order as $\hbar$ we know that Heisenberg's uncertainty relation forbids simulation of the dynamics using classical trajectories but it rather requires the atoms to be treated as wave packets. Thus $k$ will indicate in which regime the experiment is carried out. Therefore we know there is some minimum order of magnitude of $k$ which must be exceeded before we expect to see differences between quantum and classical dynamics on a given time scale.

Quantum effects can be observed only if the decoherence is kept to a minimum. The magnitude of the detuning will determine the amount of decoherence introduced into the system because the less the standing wave is detuned the more incoherent transitions (e.g., spontaneous emission) will occur. We now describe the full quantum dynamics, including spontaneous emission.

### A. The quantum master equation

Quantum mechanically, the state of the system is described by a density operator $\rho$. In order to describe spontaneous emission as well as the motion induced by the standing wave it is necessary to use a quantum master equation. Considering only motion in the direction of the standing wave, and working in the interaction picture, this is

$$\dot{\rho}=-\frac{\mathrm{i}}{\hbar}[H,\rho]+\Gamma\mathcal{L}_1\rho. \tag{6}$$

Here $H$ is the Hamiltonian for the center-of-mass and internal state of the atom, given by

$$H=\frac{p_x^2}{2m}-\hbar\delta\sigma^\dagger\sigma-\frac{\hbar}{2}[\Omega(x,t)\sigma^\dagger+\Omega^\dagger(x,t)\sigma]. \tag{7}$$

Here $\Omega(x,t)$ is the position and time-dependent Rabi-frequency operator for the atom in the standing wave and $\delta$ is the detuning of the standing wave. The atomic operators are defined in terms of $\sigma=|a\rangle\langle b|$, where $|a\rangle$ and $|b\rangle$ correspond to ground and excited states, respectively.

The superoperator $\mathcal{L}$ describes the incoherent evolution due to the coupling to the vacuum field modes at rate $\Gamma$ and is given by

$$\mathcal{L}_1=\int d^2\vec{n}\,\phi(\vec{n})\mathcal{D}[e^{ikn_x x}\sigma]. \tag{8}$$

Here $k$ is the wave number of the spontaneously emitted light, $\vec{n}$ is a unit vector describing the direction of the spontaneously emitted photon, and $\phi(\vec{n})$ is the dipole radiation distribution for this direction

$$\phi(\vec{n})=\frac{3}{8\pi}\left(1-\frac{(\vec{d}\cdot\vec{n})^2}{\vec{d}\cdot\vec{d}}\right), \tag{9}$$

where $\vec{d}$ is the atomic dipole vector. The superoperator $\mathcal{D}$ is defined for arbitrary operators $A$ and $B$ by

$$\mathcal{D}[A]B\equiv ABA^\dagger-(A^\dagger AB+BA^\dagger A)/2. \tag{10}$$

Only the $x$ component $n_x$ appears in the superoperator in Eq. (8) because we are only interested in motion in the $x$ direction. This is the direction of propagation of the light beams, so the dipole vector (which is parallel to the polarization vector of the light) is perpendicular to the $x$ direction. This enables the integral in Eq. (8) to be simplified to

$$\mathcal{L}_1=\int du\,W(u)\mathcal{D}[e^{ikux}\sigma], \tag{11}$$

where

$$W(u)=\begin{cases}\frac{3}{8}(1+u^2) & \text{for } |u|\leqslant 1\\ 0 & \text{for } |u|>1.\end{cases} \tag{12}$$

Note that $u$ can be interpreted as the $x$ component of the momentum kick to the atom, in units of $\hbar k$.

The evolution described by the master equation (6) is not obviously related to that generated by the Hamiltonian (1). For a start, the real particle is an atom with two internal states whereas the ideal particle has no internal states. To see the relation between the two models it is necessary to adiabatically eliminate the upper level of the atom. This procedure is outlined in the Appendix where we also quantify some of the approximations involved. It is valid only if the detuning $\delta$ is much greater than the maximum of the Rabi frequency $\Omega(x,t)$. In the experiment the modulated standing-wave Rabi frequency has the form

$$\Omega(x,t)=\Omega\sqrt{1-2\varepsilon\sin\omega t}\sin kx, \tag{13}$$

which gives the master equation

$$\dot{\rho}=-\frac{\mathrm{i}}{\hbar}[H,\rho]+\lambda\mathcal{L}_2\rho. \tag{14}$$

Here the Hamiltonian is

$$H=\frac{p_x^2}{2m}+\frac{\hbar\Omega_{\rm eff}}{4}(1-2\varepsilon\sin\omega t)\sin^2(kx), \tag{15}$$

which is the same as in Eq. (1), with $\Omega_{\rm eff}=\Omega^2/\delta$. The effective damping rate is $\lambda=\Gamma(\Omega/2\delta)^2$ and the superoperator $\mathcal{L}_2$ is

$$\lambda\mathcal{L}_2=\lambda\int du\, W(u)\mathcal{D}\left[e^{ikux}\sqrt{1-2\varepsilon\sin\omega t}\sin kx\right] \tag{16}$$

$$=\frac{\Gamma}{\delta}\frac{\Omega_{\rm eff}}{4}(1-2\varepsilon\sin\omega t)\int du\, W(u)\mathcal{D}[e^{ik(u+1)x}-e^{ik(u-1)x}]. \tag{17}$$

### B. Simulation methods

To obtain reliable theoretical data we have utilized two different methods to obtain our quantum simulations. The dynamics are modeled using either the master equation or quantum trajectories. These methods are inherently different. Both have been tested and found to give essentially identical results, strengthening the validity of the presented theory. To allow a comparison with classical physics we also present a method to obtain classical simulations. This will be of importance for future decoherence and quantum chaos studies.

#### *1. Simulations using the master equation*

Since the Hamiltonian (15) is periodic in $x$, it would be natural to consider using the momentum states as a basis for simulating the evolution. However, as the final expression (17) for $\mathcal{L}_2$ indicates, spontaneous emission following the absorption of a photon from the standing wave enables a transfer of momentum of any amount between $-2\hbar k$ and $+2\hbar k$ (because the momentum kick is projected onto the $x$ axis). This means that an exact one-dimensional simulation of the master equation would require a dense set of momentum states.

In practice, this dense set is not necessary as the initial conditions have a finite momentum spread which will smear out any fine structure. In fact, the initial conditions from the experimental setup have a momentum spread of order $7\hbar k$ which means that features of order $\hbar k$ are not resolvable. It therefore makes sense to approximate the continuous momentum transfer due to spontaneous emission by discrete momentum transfer in units of $\hbar k$ in order to take advantage of the symmetry of the Hamiltonian. This is achieved by replacing $\mathcal{L}_2$ by

$$\mathcal{L}_3=(1-2\varepsilon\sin\omega t)\sum_{u=-1,0,1}V(u)\mathcal{D}\left[e^{ik(u+1)x}-e^{ik(u-1)x}\right], \tag{18}$$

where $V(u)$ is a discrete approximation to $W(u)$. This is similar to the approach of Ref. [21] but is more rigorous.

Approximating $W(u)$ by $V(u)$ is not a unique procedure. Here we adopt the method of choosing $V(u)$ such that the zeroth, first, and second moments agree. That is,

$$\int W(u)\,du=1=V(-1)+V(0)+V(1), \tag{19}$$

$$\int W(u)u\,du=0=-V(-1)+V(1), \tag{20}$$

$$\int W(u)u^2\,du=\tfrac{2}{5}=V(-1)+V(1). \tag{21}$$

The first condition here is just that $V$ is normalized. The second is that $V$ reproduces the correct mean momentum kick $\langle\Delta p\rangle$ in spontaneous emission (i.e., zero). The third is that $V$ reproduces the correct mean squared momentum kick $\langle(\Delta p)^2\rangle=(2/5)(\hbar k)^2$. The three conditions imply

$$V(-1)=\tfrac{1}{5},\quad V(0)=\tfrac{3}{5},\quad V(1)=\tfrac{1}{5}. \tag{22}$$

Under this approximation, we can write the master equation in the momentum basis as

$$\dot{\rho}=-\frac{i}{\hbar}[H,\rho]+\lambda\mathcal{L}_3\rho, \tag{23}$$

where

$$H=\frac{1}{2m}\sum_n(p_0+\hbar kn)^2|n\rangle\langle n| + \frac{\hbar\Omega_{\rm eff}}{16}(1-2\varepsilon\sin\omega t)(R^2+L^2-2I), \tag{24}$$

where $|n\rangle$ is the momentum state $|p_0+\hbar kn\rangle$ (where $p_0$ is an arbitrary momentum) and

$$\mathcal{L}_3=\tfrac{1}{5}(1-2\varepsilon\sin\omega t)\{\mathcal{D}[R^2-I]+2\mathcal{D}[R-L]+\mathcal{D}[I-L^2]\}. \tag{25}$$

Here $R$ is a unitary operator (corresponding to $e^{-ikx}$) which raises the momentum by $\hbar k$, and $L$ (corresponding to $e^{ikx}$) similarly lowers it by $\hbar k$,

$$R=L^{-1}=L^{\dagger}=\sum_n|n+1\rangle\langle n|, \tag{26}$$

and $I=\Sigma_n|n\rangle\langle n|$.

Since all of the operators in the master equation (23) can be represented by matrices in the $|n\rangle$ basis, it is a simple matter to solve the equation using a suitable numerical environment such as MATLAB. The initial state matrix $\langle n|\rho(0)|n\rangle$ is found by assuming a Gaussian initial momentum distribution of $1/e$ half width of $6.5\hbar k$ which forms the diagonal elements of $\rho(0)$. To obtain smoother results a new set of momentum states is chosen, still spaced by $\hbar k$, but shifted in momentum by fractions of $\hbar k$ compared to the original set. The different density matrices are evolved and the results are combined to gain a more accurate result.

#### *2. Simulations using quantum trajectories*

Without making the approximations of adiabatic elimination of the upper level of the atom, and discretizing the

spontaneous-emission recoil, it would be numerically intractable to solve the initial master equation (6). That is because of the size of the state matrix. However, it is possible to simulate the evolution of that equation stochastically, by taking a large ensemble of quantum trajectories for the state vector. This can be done as the number of elements of the state vector is roughly equal to the square root of the number of elements of the state matrix.

The theory of quantum trajectories [22] shows that it is possible to simulate incoherent transitions using Monte Carlo methods [23], so this was done to obtain our second quantum mechanical simulations. A stochastic Schrödinger equation developed for atom optics by Dum, Zoller, and Ritsch [24] and Mølmer, Castin, and Dalibard [25] is used to include incoherent transitions.

Rather than simulate the exact dynamics of the original master equation (6) we follow Dyrting and Milburn [23] in simulating an approximate master equation. The approximate master equation is similar to that of Eq. (14) in that the atom sees a potential. However, it is potentially a better approximation than that equation because we retain the excited state of the atom $|b\rangle$. We derive this approximate master equation as Eqs. (A7) and (A8) in the Appendix, as a step along the route to deriving the master equation (14) used above. The method we use is related to, but uses different approximations from, that of Dyrting and Milburn [23].

In the quantum jump simulations the atom is always in state $|b\rangle$ or $|a\rangle$, and the potential it sees depends on which state it is in. Thus the atom has a quantum center-of-mass state $|\psi\rangle$ and an internal state which can be either $a$ or $b$ but not a superposition of both. The advantage of this approximation over the full master equation (6) is that it has a clear classical analog, as will be discussed in Sec. II B 3.

In the scaled units of Eq. (2), the stochastic equation for the state vector $|\psi\rangle$ is

$$d|\psi\rangle = -\frac{\mathrm{i}}{\hbar} d\tau K|\psi\rangle + dN_1(\tau) \times\left(\frac{\sqrt{(1-2\varepsilon\sin\tau)}\sin(q/2)}{\langle\psi|[\sqrt{(1-2\varepsilon\sin\tau)}\sin(q/2)]^2|\psi\rangle}-1\right)|\psi\rangle + dN_2(\tau)\left(\frac{\exp(\mathrm{i}\overline{pq}/\hbar)}{\sqrt{\langle\psi|\psi\rangle}}-1\right)|\psi\rangle. \tag{27}$$

Here the non-Hermitian effective Hamiltonian $K$ depends on the internal state $\sigma=a,b$ of the atom

$$K=\begin{cases} p^2/2+2\kappa(1-2\varepsilon\sin\tau)\sin^2(q/2)/\nu^* & \text{for} \quad \sigma=a \\ p^2/2-2\kappa(1-2\varepsilon\sin\tau)\sin^2(q/2)/\nu & \text{for} \quad \sigma=b \end{cases} \tag{28}$$

with

$$\nu=1-\frac{\mathrm{i}\Gamma}{2\delta}. \tag{29}$$

The imaginary part of $\nu$ makes $K$ non-Hermitian. The non-Hermitian part corresponds exactly to the anticommutator (the second term in the curly brackets) in Eqs. (A7) and (A8). It causes the modulus of the wave function to decay. This is because the smooth evolution takes into account only what happens when there are no jumps. The Hermitian part of $K$ corresponds exactly to the commutator (the first term in the curly brackets) in Eqs. (A7) and (A8). The Hermitian part of $K_a$ (for the ground state) also corresponds exactly to the Hamiltonian which appears in the final equation of the Appendix, Eq. (A12), which corresponds to the Hamiltonian of Eq. (14) in the experimentally relevant limit of $\Gamma \ll \delta$ ($\nu \approx 1$).

The point process increments $dN_1(t)$ and $dN_2(t)$ are, in any infinitesimal time increment $d\tau$, equal to either zero or one. The probabilities for the latter are equal to the expectation values of these stochastic processes and are, respectively,

$$E[dN_1]=\eta\frac{\langle\psi|(1-2\varepsilon\sin\tau)\sin^2(q/2)|\psi\rangle}{\langle\psi|\psi\rangle}d\tau, \tag{30}$$

$$E[dN_2]=(\Gamma/\omega)d\tau, \tag{31}$$

with

$$\eta=\frac{\Gamma\Omega^2}{4\omega\delta^2|\nu|^2}=\frac{\lambda}{\omega|\nu|^2}=2\times\mathrm{Im}\,\frac{2\kappa}{\hbar\nu^*}. \tag{32}$$

The jumps (when $dN_1=1$ or $dN_2=1$) cause a discontinuous change in $|\psi\rangle$ given by Eq. (27), and are accompanied by a change in the internal state of the atom as follows:

$$\begin{aligned} &a \xrightarrow{dN_1=1} b \quad \text{absorption}, \\ &b \xrightarrow{dN_1=1} a \quad \text{stimulated emission}, \\ &b \xrightarrow{dN_2=1} a \quad \text{spontaneous emission}. \end{aligned} \tag{33}$$

It is the absence of the first jump process in the smooth evolution which causes the decay in the modulus of the wave function referred to above, and from Eq. (32) it is clear that the rate of these jumps is related to the non-Hermitian part of the effective Hamiltonian $K$. When the modulus squared drops below a preset random number, a jump is assumed to occur and $dN_1(\tau)=1$. This is explained in detail in Ref. [24]. These jumps correspond to the third term in the curly brackets in Eqs. (A7) and (A8).

The second jump process (spontaneous emission) can only occur when the atom is in the excited state $b$. For as long as the atom is in the excited state, the time until a spontaneous emission has an exponential waiting time distribution with mean $\omega/\Gamma$, which is simple enough to calculate independently of the wave function modulus. This is explained in detail in Ref. [23]. These jumps correspond to the first term in Eqs. (A7) and (A8), proportional simply to $\Gamma$.

When a spontaneous emission occurs, the atom receives a random momentum kick represented by $\overline{p}$ in Eq. (27). It is given by [23]

$$\overline{p}=\hbar k \sin\phi \sin\theta, \tag{34}$$

where $\phi$ and $\theta$ are the Euler angles for the direction of spontaneous emission relative to the atomic dipole moment (which is orthogonal to the direction of motion $x$). They are generated as follows: $\phi\in[0,2\pi)$ is a random angle with uniform distribution and $\theta$ is given by

$$\theta=\arccos\left[2\cos\left(\frac{\arccos(2y-1)+4\pi}{3}\right)\right], \tag{35}$$

where $y\in[0,1]$ is a random number with uniform distribution.

For the initial states we used squeezed minimum uncertainty wave packets with a momentum width which corresponds to the experimental spread in momentum of the initial cloud. The wave packets are initially equally spaced inside one well of the standing wave. The smooth evolution part of the stochastic Schrödinger equation is solved numerically using the split-operator method [26]. In this method the nonunitary Schrödinger equation

$$i\hbar\frac{d}{d\tau}|\psi\rangle=K|\psi\rangle \tag{36}$$

has as a solution (for $\delta\tau$ short enough to neglect the time dependence of $K$) equal to

$$|\psi(\tau+\delta\tau)\rangle=\exp\left(-\frac{\mathrm{i}(T+V)\delta\tau}{\hbar}\right)|\psi(\tau)\rangle, \tag{37}$$

where $T=p^2/2$ depends only on $p$ and $V=K-T$ depends only on $q$. Using the approximation

$$\exp\left(-\frac{i(T+V)\delta\tau}{\hbar}\right)\approx\exp(-\mathrm{i}T\delta\tau/2\hbar)\exp(-\mathrm{i}V\delta\tau/\hbar)\times\exp(-\mathrm{i}T\delta\tau/2\hbar), \tag{38}$$

which is correct to order $(d\tau)^2$; the evolution can be simulated very fast by using fast Fourier transforms to transform between the momentum $p$ and position $q$ bases. An adaptive time stepsize method [27] is used to control the stepsize of the method. Once every $\varsigma$ steps the relative error $\varphi$ is calculated as

$$\varphi=\frac{\|\,|\psi_\alpha\rangle-|\psi_\beta\rangle\|}{\|\,|\psi\rangle\|}, \tag{39}$$

where

$$|\psi_\alpha\rangle=\exp(-iT\delta\tau/2\hbar)\exp(-iV\delta\tau/\hbar)\exp(-iT\delta\tau/2\hbar)|\psi\rangle, \tag{40}$$

$$|\psi_\beta\rangle=\exp(-iV\delta\tau/2\hbar)\exp(-iT\delta\tau/\hbar)\exp(-iV\delta\tau/2\hbar)|\psi\rangle. \tag{41}$$

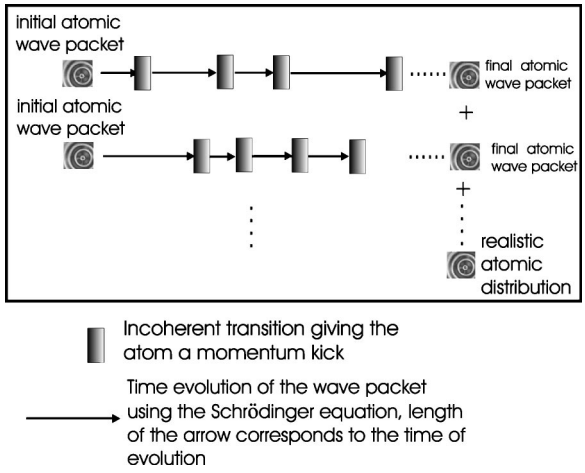


FIG. 1. Graphic representation of the quantum trajectory method.

If the error lies above a specified tolerance the simulation is restarted $\varsigma$ steps before and the step size is decreased. We have found $\varsigma=30$ to work well. This method is used to prevent unphysical behavior due to a too large relative error. Figure 1 shows a graphic representation of the method of quantum trajectories for our system.

### *3. Classical simulations*

In the classical regime one can use Hamiltons's equations to calculate the dynamics of the system. The Hamiltonian evolution of a system preserves the Poisson bracket relation between the position variable $q$ and the momentum variable $p$ [28]

$$\{q(t),p(t)\}_{q,p}=1. \tag{41}$$

To prevent unphysical behavior when using a numerical integration routine we used a symplectic integrator method which intrinsically preserves the Poisson bracket relation [29]. It was slightly changed to include time-dependent systems [33]. The Hamiltonian (which depends on the internal state of the atom) is given by

$$H_\sigma=\begin{cases}p^2/2+2\kappa(1-2\varepsilon\sin\tau)\sin^2(q/2) & \text{for}\quad \sigma=a\\ p^2/2-2\kappa(1-2\varepsilon\sin\tau)\sin^2(q/2) & \text{for}\quad \sigma=b.\end{cases} \tag{42}$$

This is identical to the non-Hermitian Hamiltonian $K_\sigma$ with $\nu$ set to unity.

To gain a realistic model incoherent transitions have been included in the classical simulation. This can be done analogously to the quantum trajectory simulations described above using a Monte Carlo simulation. The atom swaps internal states $a$ and $b$ when a jump occurs as described in Eqs. (33). The probabilities for the point process increments $dN_1$ and $dN_2$ are now given by

$$E[dN_1]=\eta(1-2\varepsilon\cos\tau)\sin^2(q/2)d\tau, \tag{43}$$

$$E[dN_2]=(\Gamma/\omega)d\tau. \tag{44}$$

When a transition takes place the position of the atom remains unchanged and the momentum is changed. When an absorption or stimulated emission takes place ($dN_2=1$) momentum of the atom changes by $\pm 1$ recoil. In case of a spontaneous emission the atom receives a random momentum kick $\overline{p}$ calculated in exactly the same way as the quantum case.

#### *4. Other theoretical considerations*

The methods presented above lead to an atomic momentum distribution resulting from the interaction of atoms with a modulated optical standing wave which is turned off and on instantaneously. To obtain more accurate results we have added into our numerical simulations the interaction due to a finite turn-on and turn-off time of the standing wave due to the experimental restrictions when using an acousto-optic modulator. The shape and length of the turn-on and turn-off were measured using a 280 MHz bandwidth photodetector. We have also found that it is important to match the beginning and end phase of the standing wave in our theoretical simulations exactly with the experimental conditions. This was also accomplished using the photodetector mentioned above.

The experimentally measured data consists of atomic position distributions after 10 ms ballistic expansion time as described in the section below. To obtain a theoretical position distribution after 10 ms, we evolve the theoretical position distribution after the standing-wave interaction for 10 ms using a propagator method. The position distribution after 10 ms turns out to be very similar to the momentum distribution straight after the standing-wave interaction as the free evolution effectively transfers all the momentum features into the position distribution. Because of this we will sometimes refer to the experimental results as momentum distributions, although they are, strictly speaking, position distributions.

Finally one needs to consider the finite position width of the initial cloud, which will contribute to the final position distribution. Therefore we convolute the final theoretical position distribution with the initial position distribution (before the standing-wave interaction) to obtain our final theoretical prediction.

## III. EXPERIMENTAL SETUP

For our experiments a standard magneto-optic trap (MOT) was used. The pressure in the vacuum chamber was around $10^{-9}$ Torr. The magnetic field coils produced a magnetic field gradient of $10^{-1}$ T/m in an anti-Helmholtz configuration. The Earth's magnetic field was zeroed using the Hanle effect [30]. When applying a magnetic field the magnitude of absorption of the laser beams changes slightly when the laser is at resonance with the atomic vapor. This can be used to zero the magnetic field with high precision. An injection-locking scheme was utilized to decrease the linewidth of the trapping diode laser down to 100 kHz, while allowing all the power of the laser to be used in the trapping experiment. Around $10^6$ rubidium atoms were polarization gradient cooled for 10 ms. This brought the atoms down to a temperature of around 8 $\mu$K. This corresponds to a $1/e$ momentum spread of 13 recoil momenta. Then the MOT was turned off but the repumping beam was left on so that the atoms accumulated in the $F=3$ ground state. After a repumping period of 500 $\mu s$ the optical standing wave was turned on. It was left on for a time corresponding to a number of periods of the modulation frequency. Both the beginning and end phases of the modulation have to be carefully chosen to ensure the visibility of the resonances. After the standing wave is switched off, the atoms undergo a period of ballistic expansion (typically 10 ms for values of $k<0.1$ and up to 16 ms for larger values of $k$). Then an image of the cloud is taken using the freezing molasses method [11,31]. In this technique the optical molasses is turned on again with the magnetic field still turned off and the resulting fluorescence is viewed with a 16 bit charge-coupled-device (CCD) camera. The CCD array of the camera was cooled, leading to a quantum efficiency of around 80% and a rms read noise of 6.7 electrons. The experimental setup is shown in Fig. 2.

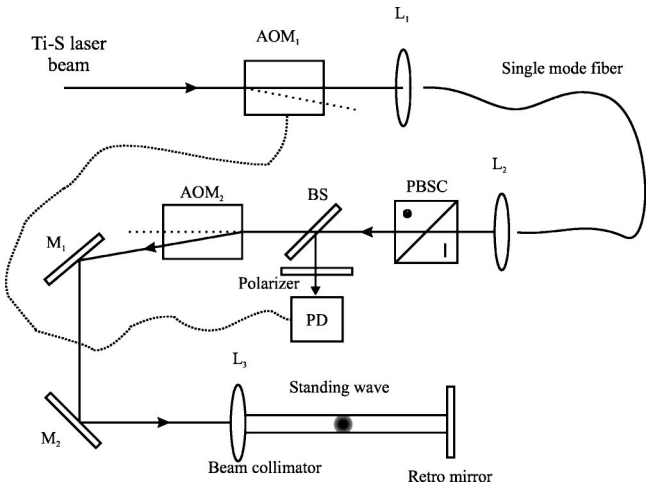


FIG. 2. Experimental setup used for our experiment. $L_1$, $L_2$ are lenses used to couple the laser beam in and out of the optical fiber which is utilized to optimize the pointing stability and to improve the quality of the laser beam. $AOM_1$ stabilizes the light intensity. $AOM_2$ produces the intensity modulation which is needed to produce an amplitude-modulated standing wave.

A frequency stabilized titanium sapphire laser produces up to 2.2 W of light at 780 nm with a linewidth of 1 MHz and a frequency drift of 50 MHz per hour. This beam is first passed through an 80-MHz acousto-optic modulator ($AOM_1$ as seen in Fig. 2) and then into a polarization-preserving single-mode optical fiber. The output beam goes through a polarizing beam-splitter cube and part of the light is fed through a polarizer to a photodetector, which gives an electronic feedback signal to the $AOM_1$ on the other end of the fiber. This reduces the standing-wave intensity noise, pointing instability and polarization noise to less than 1%. $AOM_2$ modulates the amplitude of this beam and produces an intensity modulation of the form $I_o(1-2\varepsilon \sin \omega t)$. High beam quality (Gaussian profile) after the $AOM_2$ is ensured by monitoring the beam in the far field. To test the spectral purity of our modulated standing wave the modulated light wave was observed on a fast photodetector and subsequent

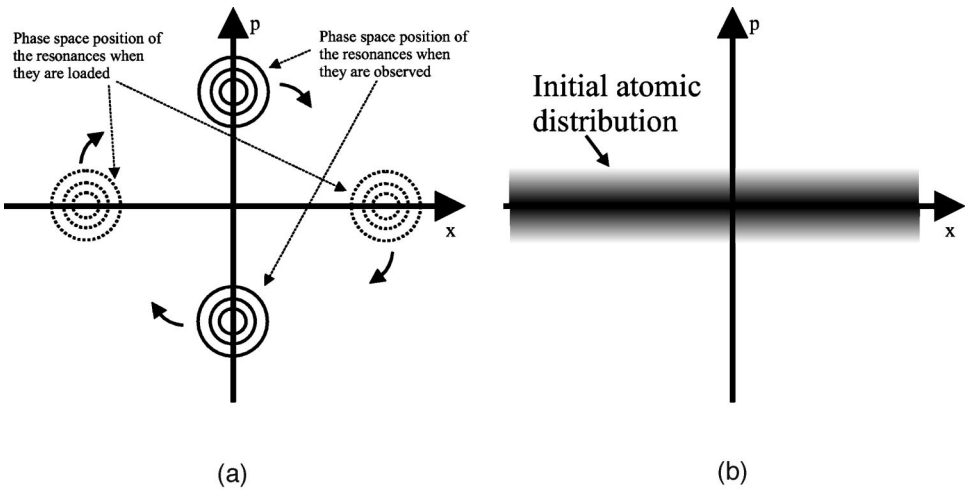


FIG. 3. The position of the resonances for loading and observation in phase space can be seen in (a). To be able to resolve the resonances using a CCD camera it is important that the resonances have maximum velocity. Therefore they should be located on the momentum axis for observation. For loading the resonances need to be located on the position axis. Part (b) shows the initial distribution of the atoms in phase space. The pictures illustrates that the resonances need to be placed on the position axis for effective loading to occur.

Fourier analysis of this signal indicated a spectral impurity of about one part in a thousand. The light after $AOM_2$ is collimated to a $1/e$ width of 2.85 mm. The beam passes through the vacuum chamber and through the atomic cloud and is retroreflected to form the one-dimensional periodic optical potential. The alignment of the retroreflection was measured to be good to approximately 0.02°. There is a variation of the scaled well depth $\kappa$ over the extent of the atomic cloud due to the Gaussian profile of our standing-wave beam. This amounts to approximately 2%. The final maximum irradiance of the standing wave in the region of the atomic cloud was $36.4 \pm 1$ W/cm$^2$. The whole experiment is computer controlled using the Labview programming environment and a general purpose interface bus (GPIB) interface.

## IV. LOADING AND OBSERVATION OF RESONANCES

Poincaré sections (stroboscopic phase-space maps) provide an easy way to understand the classical dynamics of the system. Atoms that start in a phase-space resonance rotate in phase space in time. Figure 3(a) shows the position of the resonances in phase space when they are loaded and when they are observed. The term ''phase-space resonance'' implies that the resonances rotate with an angular velocity, so that they have the same phase-space position after multiples of the modulation period. Therefore one cycle is defined as one modulation period. Furthermore, it also implies that they rotate with the same angular frequency as they would in the unmodulated case in phase space (for a period 1 resonance) [18]. The resonances are loaded when they are located on the position axis in phase space. This is easy to understand since then they overlap with the initial atomic distribution shown in Fig. 3(b). To observe the resonance experimentally one has to wait for at least a quarter cycle (period 1 resonance), so that the resonances turn 90° and are positioned on the momentum axis. When they are positioned on the momentum axis the standing wave is turned off. After a period of free evolution the momentum distribution can now be resolved experimentally by taking a picture of the atomic spatial distribution. Exact velocity measurements can be made by taking pictures of the distribution after different times and calculating the distance they have moved during that time.

One needs to wait for approximately 4.25 cycles for the dynamics of the system to settle so that the resonances can be observed. Chaotic motion needs some time to distribute atoms, which are positioned in phase space between the resonances initially, to other phase space regions where chaos persists (sea of chaos, inside the region of bounded motion). If this has occurred resonances can emerge from the background of the chaotic region.

## V. PHASE-SPACE CHARACTERIZATION UTILIZING THE MODULATION PARAMETER $\varepsilon$ AND THE DRIVING AMPLITUDE $\kappa$

Using the techniques described above we are able to provide detailed experimental analysis of size, position, and momentum of these resonances and compare experimental results with the applicable theory. For this introductory discussion we concentrate on experiments with $k=0.1$ (modulation frequency $\omega/2\pi = 300$ kHz), being close to the quantum regime, when the modulation parameter $\varepsilon$ is varied and the scaled well depth $\kappa$ is held constant ($\kappa = 1.15$). The upper part of Figure 4 shows experimental results (solid line) as well as a quantum trajectory simulations (dotted line) for the resulting atomic momentum distributions. Distinct peaks in the momentum distribution correspond to phase-space resonances. Below the experimental data, Poincaré sections for different values of the modulation parameter $\varepsilon$ illustrate the classical phase space. The Poincaré sections are taken at $n+1/4$ periods of the modulation frequency. Two islands of stability can be seen, encircled by a sea of chaos. These result from second-order resonances, which bifurcate from the origin at $\kappa = 1$. The resonance width is proportional to $\varepsilon$. However, the islands of stability break up for larger values of $\varepsilon$ and therefore do not scale with $\varepsilon$. It can be seen that the size and the shape of the center resonance and the two second-order resonances are strongly dependent on the modulation parameter. Figure 4(a) shows the unmodulated case. The region of bound motion is bound by the classical separatrix. The motion of all atoms is regular. In Fig. 4(b) two second-order resonances have emerged for $\varepsilon = 0.22$. The onset of chaotic motion can be seen. With increasing values of $\varepsilon$ the second-order resonances become more pronounced

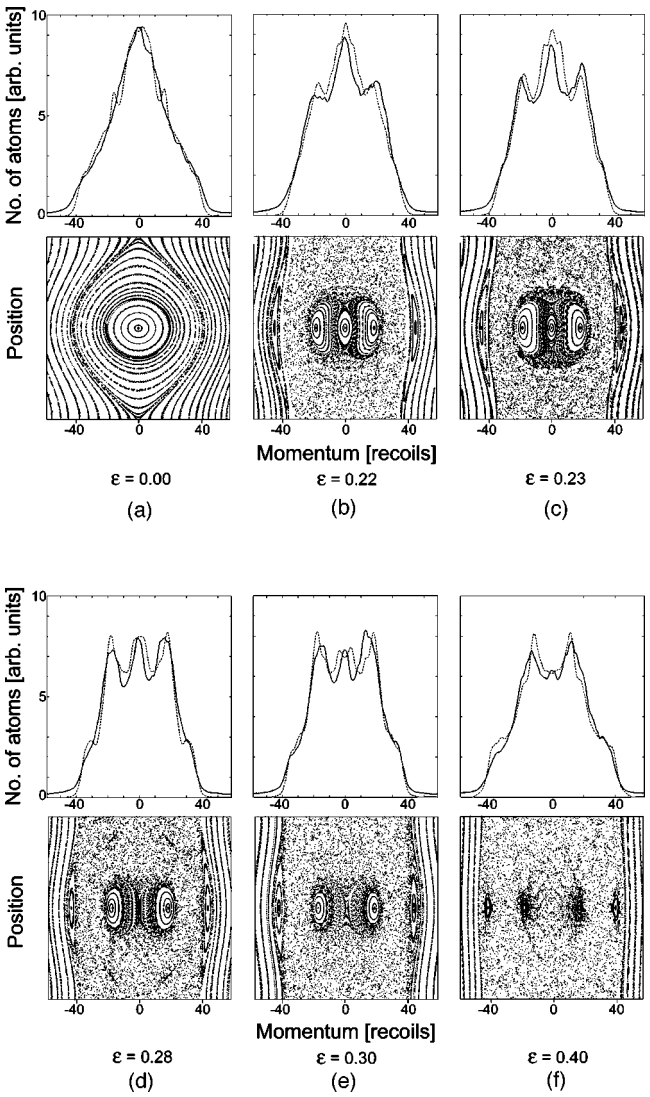


FIG. 4. The upper section shows the experimental atomic momentum distributions (solid line) together with a quantum simulation (dotted line) using the trajectory method of Sec. II B 2 for different values of the modulation amplitude $\varepsilon$. The lower part illustrates the corresponding Poincaré sections. The size of the resonances is strongly dependent on the modulation amplitude $\varepsilon$.

as can be seen in the experimental data and the quantum simulations. The region of regular motion centered at zero momentum becomes smaller and eventually disappears in the sea of chaos as can be seen in Figs. 4(d)–4(f). The small regions of regular motion positioned close to the region of unbound motion (librations) do not rotate. This means that they cannot be observed in the experiment as they need to cross the position axis to be loaded as illustrated in Fig. 3(a).

Due to the small initial momentum width, atoms are not loaded into the region of regular unbound motion. Nevertheless, chaos leads to a homogeneous spread which is confined by the region of regular unbound motion. The small shoulders visible in both experimental data and quantum simulations result from this chaotic redistribution.

We have examined the phase space for different values of the scaled driving amplitude $\kappa$. Figure 5 shows experimental results (solid line) for a range of $\kappa$ between 1.11 and 1.36 with the scaled Planck's constant $\bar{k}$ kept constant at 0.1 (modulation frequency $\omega/2\pi = 300$ kHz) and the modulation amplitude $\varepsilon$ kept constant at 0.32. This data was obtained by adjusting the detuning $\delta$ of the modulated standing wave. Alternatively an adjustment of the modulation frequency (with constant detuning) could be used to vary the scaled well depth $\kappa$ which would give similar results to that of Fig. 5. Theoretical predictions from the quantum-mechanical calculations are also shown (dotted line). The lower section of Fig. 5 contains the corresponding Poincaré sections. One can see that with changing values of $\kappa$ the velocity of the resonances is changed as is the size of the resonances. With increasing $\kappa$ the resonances become faster. We have chosen a small $\kappa$ step size between Figs. 5(a) and 5(b) to illustrate this increase in velocity without introducing a qualitative change of phase space. Figure 5(c) features the emergence of a center island. With $\kappa$ increasing even further the second-order resonances move out, become smaller as shown in Fig. 5(d), and will eventually disappear in the sea of chaos.

Slight discrepancies between quantum trajectory simulations and the experimental data could result from nonuniformities in the initial experimental position and momentum distribution. Furthermore slight errors in the alignment of the optical standing wave relative to the atomic cloud can possibly lead to discrepancies between theory and experiment. In spite of such potential problems the agreement between the experiment and theory is very good.

In the experiment we have found a maximum size of the resonances for the scaled driving amplitude $\kappa$ in a range between 1.1 and 1.3, depending on the modulation parameter $\varepsilon$ as predicted by theory. Nonlinear dynamics theory tells us that for every value of $\kappa$ there will be a modulation frequency which will be equal to the nonlinear natural frequency of the system. When this occurs the system is in resonance. However, the size of the islands of regular motion resulting from these resonances is very sensitive to system parameters $\varepsilon$ and $\kappa$. In some cases the peaks in the momentum distribution are infinitely small, while in others they form stable islands. Our simulations predict the formation of observable stable resonances for driving amplitudes in the range $\kappa = 1.0$ to 1.5. It should be noted that the variation of the scaled well depth $\kappa$ produces phase-space portraits which are similar to the ones which can be accomplished by variation of the modulation parameter $\varepsilon$.

## VI. RESONANCE MOMENTUM

While we discussed period-1 resonances in the preceding section, here we discuss the dynamics of period-2 resonances that occur at lower values of $\kappa$. This is important as for this value of $\kappa$, higher values of the modulation frequency are accessible at a detuning which is not too small to destroy the pendulum dynamics. If the detuning becomes too small the adiabatic elimination of the excited state breaks down and the center-of-mass dynamics become far more complicated. Higher resonance momenta are accessible using higher modulation frequencies. We have made momentum measure-

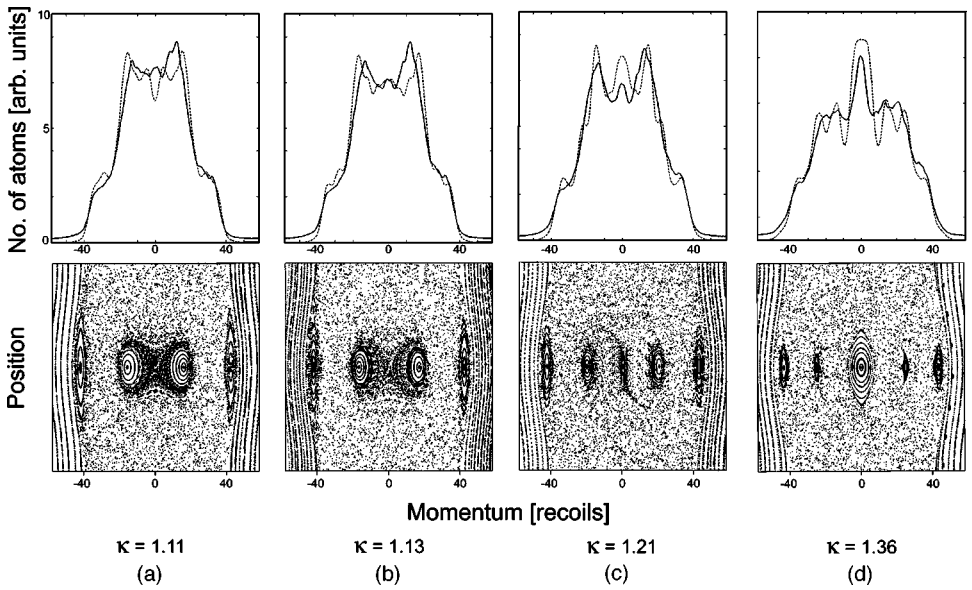


FIG. 5. Experimental data (solid line) and quantum trajectory simulation (dotted line) showing resonances as a function of the scaled driving amplitude $\kappa$. One can see that the islands of regular motion appear only for a small range of $\kappa$. The momentum of the resonances changes with $\kappa$. The corresponding Poincaré sections are shown below.

ments of the resonances for a range of modulation frequencies keeping $\kappa$ and $\varepsilon$ constant. The system can be described by the Hamiltonian given in Eq. (2). As long as $\kappa$ and $\varepsilon$ are kept constant, the resonances will appear at the same scaled momentum. The measured momentum $p_x$ of the resonances is proportional to the scaled momentum $p$ multiplied with the modulation frequency $\omega$. Therefore, the momentum of the resonances should scale linearly with modulation frequency.

For different values of the modulation frequency $\omega$, the detuning was adjusted to obtain the same value of the modulation parameter $\kappa$. Then the momentum of the resonances was measured using ballistic expansion. A graph of the experimental results is shown in Fig. 6. The resonance momenta and their errors shown are obtained from a least-squares analysis of time-of-flight data. The error bars also include the momentum error resulting from the finite width of the resonances as well as slight asymmetries in their shape. There is a linear relation between the modulation frequency and the momentum of the resonances as predicted by theory.

In fact these results can be interpreted as the experimental proof for the mapping of several different physical experiments into one unique theoretical case using scaled variables. The scaled quantum and classical theories produce a unique result for $\varepsilon$ and $\kappa$ kept constant, while the resonance momentum can be varied experimentally from 0 to many recoils by adjusting the modulation frequency $\omega$ while compensating with the detuning $\delta$.

## VII. EFFECTS OF SMALL NOISE AMPLITUDES ON THE SYSTEM

Exploring the effects of noise on an atom-optical system is of importance as the mechanisms involved are closely related to decoherence, which is an intense area of study due to its importance for the development of new quantum tech-

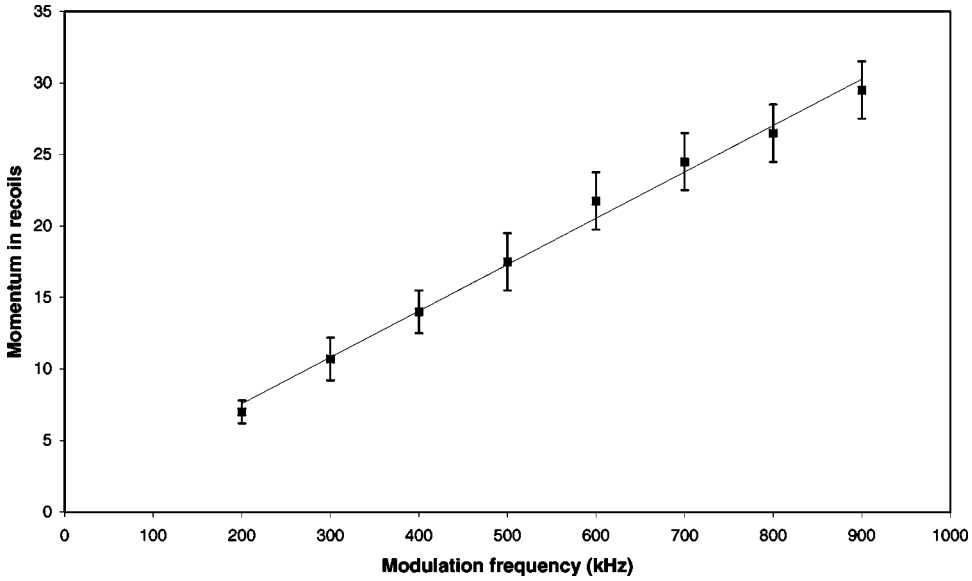


FIG. 6. Momentum of the resonances for different values of the modulation frequency $\omega/2\pi$. The modulation amplitude $\epsilon$ and the scaled well depth $\kappa$ are held constant. Results for $\epsilon = 0.32$ are shown. A linear fit is well within the error bars. This mechanism could be used for effective velocity control of atoms.

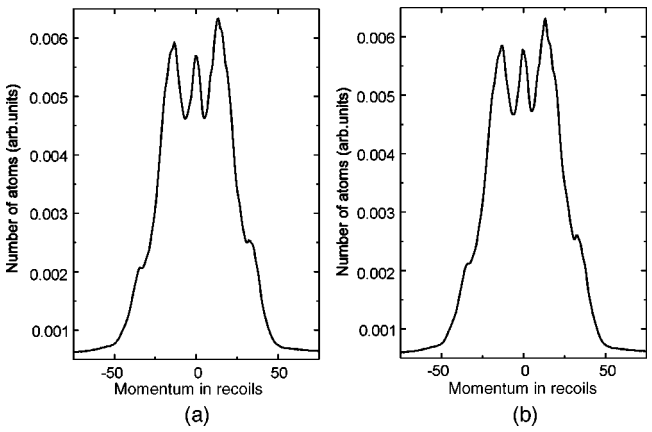


FIG. 7. Amplitude noise is introduced to the system. The resonances are remarkably stable. While there was no noise added in part (a), 10% amplitude noise was added to obtain part (b). The data was obtained at $\epsilon = 0.26$.

nologies. Goetsch and Graham have undertaken a theoretical study where they analyzed the influence of spontaneous emission on the dynamical localization in atomic momentum-transfer experiments [34]. Experiments exploring the effects of noise and dissipation on dynamical localization were carried out by Klappauf *et al.* [35] and Ammann *et al.* [12,21]. We have studied how intensity noise affects the stability and the loading of the resonances of the driven pendulum. To implement this we added noise to the modulated standing wave by adding a random number between $-1$ and 1 multiplied by both the full modulation amplitude $\kappa$ and the noise factor between 0 and 1 to every point of the modulation signal. This corresponds to adding white noise to the modulation signal. Figure 7 shows experimental results. Figure 7(a) shows the atomic distribution with no added noise. In Fig. 7(b), 10% amplitude noise (noise factor: 0.1) was added to the standing wave. Although the ratio between the height of the center resonance and the period 1 resonance changes slightly, the difference between the two cases is nearly negligible. It is remarkable that the resonances are fairly stable even with quite significant amounts of noise. Further experimental and theoretical studies of the effects when stronger noise is introduced are under way and will be reported in a future paper.

## VIII. ATOMIC MOMENTUM STATE PREPARATION

For many experiments in atom optics momentum state preparation is of significance. We have conducted preliminary experiments to achieve this goal. The final goal is to efficiently prepare atomic wave packets at a certain position in phase space with adjustable position and momentum spread. Furthermore, it might also be desirable to achieve this with a large-scaled Planck's constant and at high values of detuning to prevent decoherence due to incoherent absorption and spontaneous-emission processes. We have experimentally shown that the momentum of resonances is determined by the value of the modulation frequency when the modulation amplitude $\varepsilon$ and the modulation parameter $\kappa$ are kept constant as shown in Sec. VI. This provides the opportunity for rough momentum selection. Note that one disadvantage of this method is the fact that the momentum spread of the atoms contained in the resonances is proportional to the modulation frequency.

Furthermore, the scaled theory predicts that the momentum of the resonances is slightly dependent on the modulation amplitude $\varepsilon$ as shown in Fig. 4. The resonance momentum is also strongly dependent on the scaled well depth $\kappa$ as can be seen in Fig. 5. The disadvantage of trying to change the resonance momentum by means of changing either $\varepsilon$ or $\kappa$ is that the amount of atoms contained in the resonances as well as the size change dramatically when changing these two parameters. Therefore changing either of these parameters does not represent an efficient solution to control the momentum of an atomic ensemble.

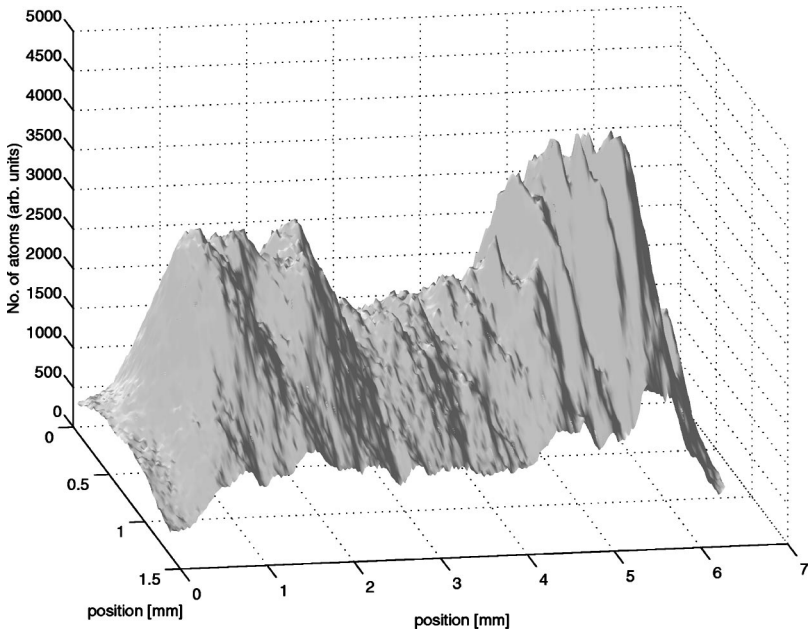


FIG. 8. Resonances of the quantum-driven pendulum. Up to around 65% of the atoms can be loaded into the resonances for effective momentum preparation. This data was obtained at a modulation parameter of 0.27 and a modulation frequency $\omega/2\pi$ of 900 kHz.

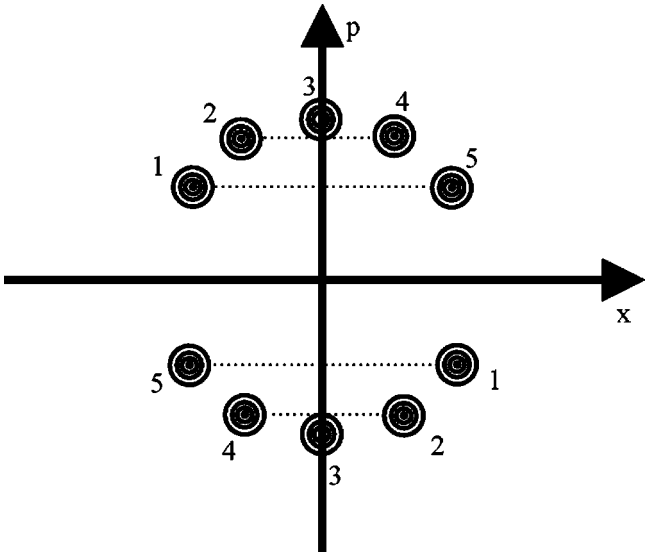


FIG. 9. Rather than turning the standing wave off when the resonances are positioned on the momentum axis (position 3), the standing wave can be turned off slightly before or after that time. This corresponds to a rotation of the resonances by up to 45° (positions 1,2,4,5) in phase space. Note the symmetry of positions 2 and 4, 1 and 5.

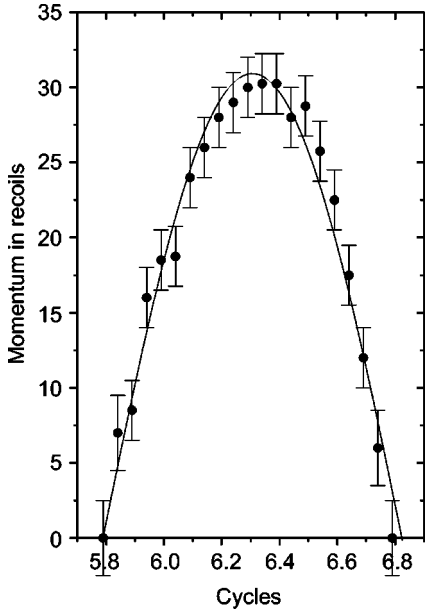


FIG. 10. Experimental data showing the momentum of the resonances for different end phases of the modulated standing wave. 6.37 cycles correspond to turning off the standing wave at a modulation minimum. The data shown here were obtained at a modulation frequency $\omega/2\pi$ of 900 kHz and a modulation parameter of 0.27. A sinusoidal fit is within the error bars.

We have found a far more efficient way to control the momentum of an atomic ensemble while preserving atomic coherence. Choosing the right parameters one can load up to 65% of all atoms into the resonances. Figure 8 shows an experimental atomic position distribution after 10-ms ballistic expansion time. Here the two resonances were measured to move with a momentum of 30.25 recoils. This method does not rely on changing any of the parameters $\kappa$, $\bar{k}$, or $\varepsilon$. The velocity of the resonances can be well controlled by changing the end phase of the modulation of the standing wave. In this method we stop the modulation of the standing wave at different times, not necessarily when the resonances are positioned on the momentum axis. This corresponds to a rotation of the resonances by up to 45° from the observation position on the momentum axis as can be seen in Fig. 9. We have achieved a velocity range of 35 recoils with this method which could be even further extended by increasing the modulation frequency. Figure 10 shows the experimentally obtained velocities for different end phases of the modulation signal. The curve is approximately symmetric around 6.37 cycles at which the resonances are positioned on the momentum axis. We have included a sinusoidal fit to show that this velocity control mechanism can be explained by the rotation of the resonances in phase space. Note the two-cycle symmetry of this experiment, due to the fact that the resonances which are utilized are period-2 resonances.

## IX. CONCLUSION

Atom optics is an ideal experimental setting to explore the quantum driven pendulum and its classical analog. The dynamics are best understood from a quantum chaotic phase space or the classical analog, depending at which value of the scaled Planck's constant $\bar{k}$ the experiment is performed. In this paper we have presented experimental results and theoretical techniques pertaining to this system.

We have given a thorough experimental investigation of the quantum chaotic phase space of the driven pendulum in atom optics. We have characterized parts of the parameter space that determine the observed phase-space dynamics. We presented experimental evidence for how the size and amplitude of these resonances depend on the modulation frequency, the scaled well depth, the modulation amplitude and the scaled Planck's constant of the system. With the appropriate choice of parameters even the central island of stability can be eliminated while retaining the second-order resonances. We have given experimental proof that the described experimental system used can be accurately modeled by the theory which we have provided here. We have developed two experimental methods in which the momentum of these resonances can be controlled very accurately. One of the methods allows us to fine tune the momentum of resonances. Experimental evidence for the accuracy and efficiency of this method is given. In contrast to changing the modulation frequency as a means for momentum control this method leaves the momentum width of the resonances unchanged. We have investigated the effect of small-noise amplitudes on this quantum chaotic system and found surprising stability.

In addition we have shown that the quantum chaotic mixed phase space provides a range of possibilities for effective quantum phase-space preparation. The results presented here are likely to be useful for atom interferometry, Bragg scattering, and perhaps even the coherent splitting of a Bose-Einstein condensate and other areas of atom optics. We have shown that up to approximately 65% of all atoms can

be loaded into the resonances, allowing efficient atomic velocity control.

Due to the control of the scaled Planck constant this experiment provides an ideal environment for studies of quantum chaos and decoherence. Analyzing the driven pendulum in atom optics is an effective means to explore the borderland between quantum and classical physics as the experiments illustrate that one needs to consider the wave nature of atoms to accurately explain the atomic dynamics.

Further investigation is in progress addressing quantum phenomena which can occur in this system, some of which are predicted by Dyrting, Milburn, and Holmes [18] and Sanders and Milburn [32].

## ACKNOWLEDGMENTS

The corresponding author W.K.H. would like to thank Gerard Milburn and Cathy Holmes for some very helpful discussions as well as Howard Carmichael for some interesting discussions concerning quantum trajectories. H.M.W. would like to acknowledge enlightening discussions with Prahlad Warszawski. This work is supported by the Australian Research Council.

## APPENDIX: ADIABATIC ELIMINATION OF THE UPPER STATE

The adiabatic elimination technique we use here is similar to that introduced by Graham, Schlautmann, and Zoller [10] for the same system, but we give a more complete derivation including justifications for the approximations made using the parameters of the experiment. We also relate the equations to those of Dyrting and Milburn [23], derived using a different technique, which are the basis for the quantum trajectory simulations of this paper.

We can write the master equation for the two-level atom in a light field as

$$\dot{\rho}=\Gamma\left(\mathcal{B}\sigma\rho\sigma^{\dagger}-\frac{1}{2}\{\sigma^{\dagger}\sigma,\rho\}\right)-\frac{\mathrm{i}}{2}[\Omega(x,t)\sigma^{\dagger}+\sigma\Omega^{\dagger}(x,t),\rho]$$
$$-\mathrm{i}\delta[\sigma^{\dagger}\sigma,\rho]-\frac{\mathrm{i}}{2\hbar m}[p^2,\rho], \tag{A1}$$

where for an arbitrary operator $R$

$$\mathcal{B}R=\int d^2\vec{n}\,\phi(\vec{n})e^{ikn_x x}Re^{-ikn_x x}. \tag{A2}$$

Explicitly using the internal state basis $a,b$ we have

$$\dot{\rho}_{aa}=\Gamma\mathcal{B}\rho_{bb}-\frac{\mathrm{i}}{2}[\Omega^{\dagger}(x,t)\rho_{ba}-\rho_{ab}\Omega(x,t)]$$
$$-\frac{\mathrm{i}}{2\hbar m}[p^2,\rho_{aa}], \tag{A3}$$

$$\dot{\rho}_{ab}=-\frac{\Gamma}{2}\rho_{ab}-\frac{\mathrm{i}}{2}[\Omega^{\dagger}(x,t)\rho_{bb}-\rho_{aa}\Omega^{\dagger}(x,t)]$$
$$+\mathrm{i}\delta\rho_{ab}-\frac{\mathrm{i}}{2\hbar m}[p^2,\rho_{ab}], \tag{A4}$$

$$\dot{\rho}_{bb}=-\Gamma\rho_{bb}-\frac{\mathrm{i}}{2}[\Omega(x,t)\rho_{ab}-\rho_{ba}\Omega^{\dagger}(x,t)]$$
$$-\frac{\mathrm{i}}{2\hbar m}[p^2,\rho_{bb}]. \tag{A5}$$

Now in the experiment $|\Omega(x,t)|\lesssim\Omega\approx 4.65\times10^9\ \mathrm{s}^{-1}$, and $\delta\approx 7$ GHz ($\delta\approx 44\times10^9\ \mathrm{s}^{-1}$). Thus we are always in the well-detuned regime where $\Omega\ll\delta$. As a result, most of the time the atom will be in the ground state with $\rho_{bb}\sim(\Omega/\delta)^2$, as we will show. As long as we are not interested in evolution faster than the time scale $\Gamma^{-1}$, we can then slave $\rho_{ab}$ and $\rho_{bb}$ to $\rho_{aa}$. Specifically, we see from Eq. (A4) that $\rho_{ab}$ will quickly come to equilibrium (at rate $\Gamma/2$) with respect to the value of $\rho_{aa}$, which evolves slowly. Setting $\dot{\rho}_{ab}=0$ thus gives

$$\rho_{ab}\simeq\frac{\mathrm{i}[\rho_{aa}\Omega^{\dagger}(x,t)-\Omega^{\dagger}(x,t)\rho_{bb}]}{\Gamma-2\mathrm{i}\delta}. \tag{A6}$$

Since $\Omega(x,t)$ is time dependent, this expression can only be valid if the rate of decay, $\Gamma/2$, is much greater than the rate of variation of $\Omega(x,t)$. In the experiment $\Gamma/2\simeq 19\times10^6\ \mathrm{s}^{-1}$ while the angular modulation frequency is typically an order of magnitude smaller. In deriving Eq. (A6) we have also assumed that the kinetic energy is much less than $\hbar\delta$ and $\hbar\Gamma$ and so can be ignored compared to them. In the experiment $\delta\approx 44\times10^9\ \mathrm{s}^{-1}$, $\Gamma\simeq 3.8\times10^7\ \mathrm{s}^{-1}$, and the recoil frequency is $3.8\times10^3\ \mathrm{s}^{-1}$. Since the $1/e$ momentum half-width is of order 7 recoil momenta, the kinetic energy divided by $\hbar$ is of order $10^5\ \mathrm{s}^{-1}$. Thus the above assumptions are justified.

Substituting Eq. (A6) into Eq. (A5) and Eq. (A3) give the following coupled equations:

$$\dot{\rho}_{aa}=\Gamma\mathcal{B}\rho_{bb}+\frac{1}{\Gamma^2+4\delta^2}\{i\delta[\Omega^{\dagger}(x,t)\Omega(x,t),\rho_{aa}]$$
$$-\Gamma\{\Omega^{\dagger}(x,t)\Omega(x,t),\rho_{aa}\}/2+\Gamma\Omega^{\dagger}(x,t)\rho_{bb}\Omega(x,t)\}$$
$$-\frac{\mathrm{i}}{2\hbar m}[p^2,\rho_{aa}], \tag{A7}$$

$$\dot{\rho}_{bb}=-\Gamma\rho_{bb}+\frac{1}{\Gamma^2+4\delta^2}\{-i\delta[\Omega(x,t)\Omega^{\dagger}(x,t),\rho_{bb}]$$
$$-\Gamma\{\Omega(x,t)\Omega^{\dagger}(x,t),\rho_{bb}\}/2+\Gamma\Omega(x,t)\rho_{aa}\Omega^{\dagger}(x,t)\}$$
$$-\frac{\mathrm{i}}{2\hbar m}[p^2,\rho_{bb}]. \tag{A8}$$

These are the equations which are simulated by the quantum trajectories in Sec. II B 2.

We can simplify the system still further by adiabatically eliminating the upper state $\rho_{bb}$, by setting $\dot{\rho}_{bb}=0$. This requires that the damping rate $\Gamma$ be much greater than the rate of variation of $\Omega(x,t)$ and the kinetic energy divided by $\hbar$. These are the same approximations as used above in deriving Eq. (A6). Strictly, this technique also requires that $\Gamma$ be much greater than $\Omega^2/\delta$, which is not satisfied for our system. It can be shown that a more rigorous approach to adiabatic elimination [36] removes this requirement, and gives a slightly different result in the end. This is based on moving into the interaction picture with respect to the ground-state potential $H_0=(\hbar/4\delta)\Omega(x,t)\Omega^\dagger(x,t)$ (which results from the adiabatic elimination) before beginning the adiabatic elimination. It does not yield the above Dyrting-Milburn equations which are the basis for our quantum trajectory simulations. For this reason, and because the correction to our final master equation is small, we will continue to follow the simpler procedure we have used so far.

Slaving $\rho_{bb}$ to $\rho_{aa}$ by setting $\dot{\rho}_{bb}=0$ gives

$$\rho_{bb}+\frac{\{\Omega(x,t)\Omega^\dagger(x,t),\rho_{bb}\}/2+i(\delta/\Gamma)[\Omega(x,t)\Omega^\dagger(x,t),\rho_{bb}]}{\Gamma^2+4\delta^2}\simeq\frac{\Omega(x,t)\rho_{aa}\Omega^\dagger(x,t)}{\Gamma^2+4\delta^2}. \tag{A9}$$

The first correction term on the left-hand side (LHS) (the anticommutator) scales like $\Omega^2/4\delta^2$, which is, as we have shown above, negligible. The second correction term on the LHS (the commutator) cannot be removed so simply, since (as noted above) the experimental parameters do not satisfy $\Gamma\gg\Omega^2/\delta$. In the more sophisticated treatment of making the adiabatic approximation in an interaction picture, this term does not appear. Knowing this, we can justify dropping it here. Thus we arrive at the simple expression

$$\rho_{bb}\simeq\frac{\Omega^\dagger(x,t)\rho_{aa}\Omega(x,t)}{\Gamma^2+4\delta^2}, \tag{A10}$$

which scales as $(\Omega/\delta)^2$ as claimed.

The reduced density operator for the center-of-mass alone is given by the partial trace over the internal atomic states:

$$\rho_{\mathrm{com}}=\mathrm{Tr}_{\mathrm{int}}\rho=\rho_{aa}+\rho_{bb} \tag{A11}$$

Denoting $\rho_{\mathrm{com}}$ simply as $\rho$, the above scaling implies that $\rho\simeq\rho_{aa}$. Using this, and substituting the above expression for $\rho_{bb}$ into Eq. (A3) gives finally

$$\dot{\rho}=\frac{\Gamma}{\Gamma^2+4\delta^2}\left(\mathcal{B}\Omega^\dagger(x,t)\rho\Omega(x,t)-\frac{1}{2}\{\Omega(x,t)\Omega^\dagger(x,t),\rho\}\right)$$
$$-\mathrm{i}\frac{\delta}{\Gamma^2+4\delta^2}[\Omega(x,t)\Omega^\dagger(x,t),\rho]-\frac{\mathrm{i}}{2\hbar m}[p^2,\rho]. \tag{A12}$$

For $\delta\gg\Gamma$ this is identical to Eq. (14). The more sophisticated adiabatic elimination would produce an extra Hamiltonian term scaling as $\Omega^4/\delta^3$. For the experimental parameters, this is only about 1% as large as the dominant Hamiltonian term scaling as $\Omega^2/\delta$, and can thus be safely ignored.


[1] A. Einstein, Verh. Dtsch. Phys. Ges. **19**, 82 (1917).
[2] M.V. Berry. Proc. R. Soc. London, Ser. A **413**, 183 (1987).
[3] K. Nakamura, *Quantum versus Chaos. Questions Emerging from Mesoscopic Cosmos* (Kluwer Academic, Dordrecht, 1997).
[4] S. Fishman, D.R. Grempel, and R.E. Prange, Phys. Rev. Lett. **49**, 509 (1982).
[5] C.M. Marcus, A.J. Rimberg, R.M. Westervelt, P.F. Hopkins, and A.C. Gossard, Phys. Rev. Lett. **69**, 506 (1992).
[6] R. Blumel, S. Fishman, and U. Smilansky, J. Chem. Phys. **84**, 2604 (1986).
[7] S. Sridhar. Phys. Rev. Lett. **67**, 785 (1991).
[8] J.E. Bayfield and P.M. Koch, Phys. Rev. Lett. **33**, 258 (1974).
[9] R.V. Jensen, S.M. Susskind, and M.M. Sanders, Phys. Rep. **201**, 1 (1991).
[10] R. Graham, M. Schlautmann, and P. Zoller, Phys. Rev. A **45**, R19 (1992).
[11] F.L. Moore, J.C. Robinson, C.F. Bharucha, B. Sundaram, and M.G. Raizen, Phys. Rev. Lett. **75**, 4598 (1995).
[12] H. Ammann, R. Gray, I. Shvarchuck, and N. Christensen, Phys. Rev. Lett. **80**, 4111 (1998).
[13] F. L. Moore, J. C. Robinson, C. Bharucha, P. E. Williams, and M. G. Raizen, Phys. Rev. Lett. **73**, 2974 (1994).
[14] J.C. Robinson, C. Bharucha, F.L. Moore, R. Jahnke, G.A. Georgakis, Q. Niu, M.G. Raizen, and Bala Sundaram, Phys. Rev. Lett. **74**, 3963 (1995).
[15] R.M. Sinclair, J.C. Hosea, and G.V. Sheffield, Rev. Sci. Instrum. **41**, 1552 (1970).
[16] J. Chaiken, R. Chevray, M. Tabor, and Q.M. Tan, Proc. R. Soc. London, Ser. A **408**, 165 (1986).
[17] J.E. Bayfield and David S. Sokol, Phys. Rev. Lett. **61**, 2007 (1988).
[18] S. Dyrting, G.J. Milburn, and C.A. Holmes, Phys. Rev. E **48**, 969 (1993).

[19] M. Hug and G.J. Milburn, Phys. Rev. A **63**, 023413 (2001).
[20] W. Chen, S. Dyrting, G.J. Milburn, Aust. J. Phys. **49**, 777 (1996).
[21] G.H. Ball, K.M.D. Vant, H. Ammann, and N.L. Christensen, J. Opt. B: Quantum Semiclassical Opt. **1**, 357 (1999).
[22] H.J. Charmichael, *An Open Systems Approach to Quantum Optics* (Springer-Verlag, Berlin, 1993).
[23] S. Dyrting and G.J. Milburn, Phys. Rev. A **51**, 3136 (1995).
[24] R. Dum, P. Zoller, and H. Ritch, Phys. Rev. A **45**, 4879 (1992).
[25] K. Mølmer, Y. Castin and J. Dalibard, J. Opt. Soc. Am. B **10**, 524 (1993).
[26] M.D. Feit, J.A. Fleck, Jr., and A. Steiger, J. Comput. Phys. **47**, 412 (1982).
[27] S.M. Tan and D.F. Walls, J. Phys. II **4**, 1897 (1994).
[28] R.D. Ruth, IEEE Trans. Nucl. Sci. **NS-30**, 2669 (1983).
[29] E. Forest and M. Berz, in *Lie Methods in Optics II*, edited by K.B. Wolf (Springer-Verlag, Berlin, 1989), p. 47.
[30] J. Dupont-Roc, S. Haroche, and C. Cohen-Tannoudji, Phys. Lett. A **28A**, 638 (1969).
[31] A.G. Truscott, D. Baleva, N.R. Heckenberg, and H. Rubinsztein-Dunlop, Opt. Commun. **145**, 81 (1998).
[32] B.C. Sanders and G.J. Milburn, Z. Phys. B: **77**, 497 (1989).
[33] S. Dyrting, Ph.D. thesis, The University of Queensland, 1994.
[34] P. Goetsch and R. Graham, Phys. Rev. A **54**, 5345 (1996).
[35] B. G. Klappauf, W. H. Oskay, D. A. Steck, and M. G. Raizen, Phys. Rev. Lett. **81**, 1203 (1998).
[36] P. Warszawksi and H.M. Wiseman, Phys. Rev. A **63**, 013803 (2000).